An Eight-Month Sample of Marine Stratocumulus Cloud Fraction, Albedo, and Integrated Liquid Water

C. W. FAIRALL AND J. E. HARE

Department of Meteorology, Pennsylvania State University, University Park, Pennsylvania

J. B. SNIDER

NOAA/ERL/WPL, Boulder, Colorado

(Manuscript received 15 August 1989, in final form 26 January 1990)

ABSTRACT

As part of the First International Satellite Cloud Climatology Regional Experiment (FIRE), a surface meteorology and shortwave/longwave irradiance station was operated in a marine stratocumulus regime on the northwest tip of San Nicolas Island off the coast of Southern California. Measurements were taken from March through October 1987, including a FIRE Intensive Field Operation (IFO) held in July. Algorithms were developed to use the longwave irradiance data to estimate fractional cloudiness and to use the shortwave irradiance to estimate cloud albedo and integrated cloud liquid water content. Cloud base height is estimated from computations of the lifting condensation level. The algorithms are tested against direct measurements made during the IFO; a 30% adjustment was made to the liquid water parameterization. The algorithms are then applied to the entire database. The stratocumulus clouds over the island are found to have a cloud base height of about 400 m, an integrated liquid water content of 75 gm^{-2}, a fractional cloudiness of 0.95, and an albedo of 0.55. Integrated liquid water content rarely exceeds 350 g m^{-2} and albedo rarely exceeds 0.90 for stratocumulus clouds. Over the summer months, the average cloud fraction shows a maximum at sunrise of 0.74 and a minimum at sunset of 0.41. Over the same period, the average cloud albedo shows a maximum of 0.61 at sunrise and a minimum of 0.31 a few hours after local noon (although the estimate is more uncertain because of the extreme solar zenith angle). The use of joint frequency distributions of fractional cloudiness with solar transmittance or cloud base height to classify cloud types appears to be useful.

1. Introduction

Because of their high albedo relative to the ocean surface and close coupling to the ocean surface temperature, marine stratocumulus clouds have a large influence on the radiation balance over the oceans. This is often referred to as the "albedo effect." Randall et al. (1984) suggest that a 4% increase in the area of the globe covered by these clouds would offset the 2–3 K rise predicted in global temperature due to a doubling of atmospheric CO_2. Furthermore, the radiative transfer properties of stratocumulus clouds are moderately sensitive to their microphysical state. Charlson et al. (1987) have suggested that stratocumulus albedo sensitivity to cloud condensation nuclei (CCN) concentrations may provide a mechanism for biological modulation of global climate. It has also been long recognized that stratocumulus clouds have a strong influence on marine boundary layer dynamics (e.g., the classic treatment by Lilly 1968), primarily through production of turbulence by cloud top radiative cooling. Thus, proper treatment of stratocumulus clouds is important in atmospheric models from the boundary layer scale to general circulation models (GCMs) used to simulate global climate (Randall 1985).

Our understanding of marine stratocumulus is based on a combination of observations and theoretical reasoning. Until recently the historical records of marine cloud properties consisted primarily of eyeball estimates of cloud type and amount made from coastal stations, islands, and a few ships. The last few decades have seen various types of instrumented aircraft used to probe the clouds directly and a bewildering variety of numerical simulations used to investigate stratocumulus microphysical and micrometeorological processes (see the summary in Randall et al. 1984). Surface-based remote sensors are just now being applied in this area (e.g., Albrecht et al. 1988; Albrecht et al. 1990). Satellite observations are also being used to examine stratocumulus properties from a perspective more compatible with GCM scales (Coakley and Baldwin 1984; Minnis and Wielicki 1988) and to deduce

Corresponding author address: Dr. C. W. Fairall, R/E/WP7, NOAA/ERL, 325 Broadway, Boulder, CO 80303.

the effect of clouds on the surface radiation budget (Gautier et al. 1980; Frouin et al. 1988). While satellites are still the best approach for obtaining a global climatology of stratocumulus properties, it is probably unrealistic to assume that all relevant cloud properties can be deduced from satellite measured radiances. This, plus the known difficulties associated with verifying satellite/cloud/radiance algorithms by comparison with local in situ measurements, suggests the need for a program of surface-based measurements of radiances and irradiances on time scales appropriate for constructing climatologies and comparing with satellite data.

To promote understanding of clouds and improve climate-scale modeling of clouds, the First International Satellite Cloud Climatology Project Regional Experiment (FIRE) was organized (Randall et al. 1984; Cox et al. 1987). The FIRE program features a combination of intensive field observations (IFO) conducted during campaigns of relatively limited duration (on the order of one month) and extended time/space observations (ETO). The ETO program consists of satellite and surface-based measurements. As part of the FIRE/ETO program, extended time observations were made at San Nicolas Island (SNI) from March to October 1987. A small ground station was installed at the northwest tip of SNI, which is dominated by marine flow most of the time. Hourly averages of air temperature, relative humidity, wind speed and direction, solar irradiance, and downward longwave irradiance were recorded. The radiation sensors were standard Eppley pyranometers (shortwave) and pyrgeometers (longwave). San Nicolas Island also served as the focus of the first stratocumulus IFO during July 1987 (Albrecht et al. 1988).

The SNI data have been processed in several ways to deduce properties of the stratocumulus covered marine boundary layer (MBL). For example, from the temperature and humidity the lifting condensation level, which is an estimate of the height of the cloud bottom, can be computed. A combination of longwave irradiance statistics (mean and standard deviation) can be used to estimate fractional cloud cover. We will also describe an analysis technique used to estimate the integrated cloud liquid water content (W) and the cloud albedo from the measured solar irradiance. In this approach, the cloud transmittance is computed by dividing the irradiance measured at some time by a clear sky value obtained at the same hour on a cloudless day. From the transmittance and the zenith angle, values of cloud albedo and optical thickness are computed using the radiative transfer parameterizations of Stephens (1978). The integrated liquid water content is computed from the optical thickness using a variation of the Stephens' parameterization that is optimized for stratocumulus clouds. These analysis algorithms have been evaluated with 17 days of simultaneous and colocated mm-wave (20.6 and 31.65 GHz) radiometer measurements of W and lidar ceilometer measurements of cloud fraction and cloud base height made during the FIRE IFO. The algorithms are then applied to the entire dataset to produce a climatology of these cloud properties for the eight-month period.

This paper is organized as follows: experimental details are summarized in section 2, the application of the Stephens (1978) model and the shortwave algorithm is described in section 3 and evaluated in section 4, and the longwave algorithm for fractional cloudiness is described in section 5 and evaluated in section 6. The algorithms are applied to the entire 8-month dataset and the climatological results are given in section 7; conclusions are given in section 8.

2. Experimental details

San Nicolas Island is located approximately 100 km southwest of Los Angeles, California (Fig. 1). The island is owned by the U.S. Navy, where a small base (airport, harbor, housing, etc.) is maintained primarily for radar tracking operations associated with the activities of the Pacific Missile Test Center (PMTC) in Pt. Mugu, California. Both the ETO and IFO programs were conducted from the northwest tip of the island (33°16′37″ north, 119°34′34″ west) which, due to the prevailing winds, is situated in a classic MBL regime more than 50% of the time (Blanc 1981). SNI has served as the focal point for a number of MBL studies in the past (e.g., Davidson et al. 1984). The sensors used for the ETO were mounted on a small scaffold and the data acquisition equipment was located in a nearby trailer. A Campbell model 21X data logger was used. The sensors were sampled about once per second; half-hour mean and standard deviations were stored. The data logger was periodically (every few weeks) interrogated and the data transferred to Penn State via telephone lines using standard modems. For the study described here, the data were further reduced to one-hour averages.

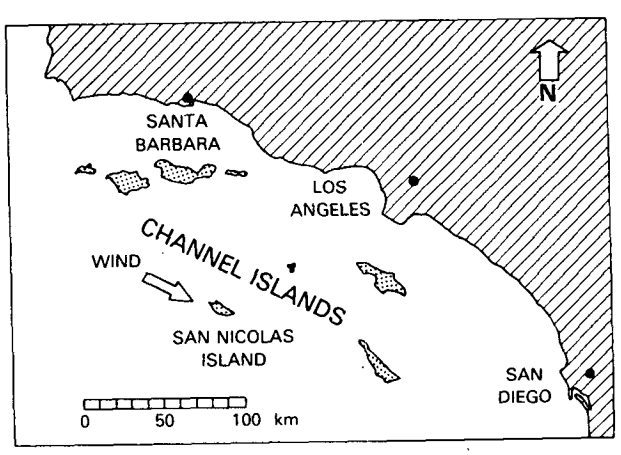

FIG. 1. Location of San Nicolas Island in the Los Angeles basin.

TABLE 1. Instrumentation and specifications for the San Nicolas Island measurements.

Variable	Sensor type	Manufacturer/model	Accuracy
Air temperature (T)	Thermistor	Rotronic MP-100	0.5 K*
Relative humidity (RH)	Hygristor	Rotronic MP-100	5%
Wind speed (u)	Cup anemometer	RM Young wind sentry	5%
Wind direction (ϕ)	Vane	RM Young wind sentry	5 deg.
Longwave irradiance (R_L)	Pyrgeometer	Eppley PIR	5 W m^{-2}
Solar irradiance (R_S)	Pyranometer	Eppley PSP	3%

* The sensor is accurate to 0.1 K; this value is an estimate of the inadequacy of the radiation shield.

Conventional meteorological sensors (see Table 1) were used; the specific sensors were selected based on our perception of their ability to withstand several months exposure to the harsh marine environment. The pyranometer has a standard Schott glass dome that is transparent in the 0.28 to 3 μm wavelength range. The pyrgeometer has a silicon dome that is transparent in the 4 to 50 μm wavelength range. Because the radiative flux measurements are considered key to this project, special steps were taken to ensure their data quality. The radiation sensors were deployed in pairs: one sensor was left exposed continuously and provided the basic measurements; the other sensor, which was kept covered except for occasional comparison periods, served as a calibration standard to monitor the possible deterioration of the continuously exposed sensor. Every few weeks, the measurements standard sensor was exposed for about 24 hours and its data also recorded. Afterwards, the standard was covered and the dome of the continuously exposed sensor was cleaned. The maximum disagreement of the pyranometers was no more than a few percent and the pyrgeometers no more than 5 W m^2. Surprisingly, the agreement remained about the same throughout the experiment. The major environmental damage was substantial corrosion of the metal body parts and the electrical connectors.

A complete description of the FIRE IFO has been given by Albrecht et al. (1988), so only a brief sketch will be given here. The experiment lasted from 29 June to 19 July 1987. The island instrumentation included a meteorological tower, two tethered balloons, a three-channel microwave radiometer, an acoustic radar, a UHF wind profiler, various radiation sensors, rawinsondes, and a lidar ceilometer. Further discussion of the ceilometer and the microwave radiometer will be given here because their data are used in this study.

The ceilometer, a Vaisala model CT 12K, is a lidar instrument operating at a wavelength of 0.904 μm. A cloud base height measurement is obtained approximately every 30 s with a vertical resolution of 15 m up to a maximum altitude of 3.66 km. The ceilometer contains an internal microprocessor that analyzes the intensity of the return, determines the cloud base height, and outputs a data message on a serial port. This information was acquired and archived with a PC type computer (Schubert et al. 1987). Low-cloud fraction is also easily computed from the time series of the ceilometer information as the fraction of time a cloud base was observed in some specified time interval (e.g., one hour).

The microwave radiometer employed at SNI during the FIRE IFO is a three-frequency system for the simultaneous measurement at atmospheric water vapor and liquid water in clouds; details of the system are given in Hogg et al. (1983). The system is completely passive, utilizing the natural emission of microwave energy by water vapor and liquid water. Measured values are total liquid water and water vapor integrated along the atmospheric path being observed by the radiometer antenna beam. The system contains three independent channels: the first operates at a wavelength of 1.46 cm (20.6 GHz) which is sensitive primarily to water vapor; the second operates at a wavelength of 0.95 cm (31.65 GHz) which is sensitive primarily to liquid water; the third operates at a wavelength of 0.33 cm (90.0 GHz) which is sensitive to both vapor and liquid. However, the third channel is approximately six times more sensitive to liquid water than is the second channel. The three radiometers are coupled into a common antenna system with concentric beams of equal 2.5 deg width. Although the antenna system is steerable in both azimuth and elevation, the antenna beams were directed only to the zenith for the period of the IFO.

Because of uncertainties in the formulation of absorption by water vapor at the 0.33 cm wavelength, data from only the 1.46 cm and 0.95 cm channels are used to retrieve vapor and liquid values. The statistical retrieval technique is described in Hogg et al. (1983). The estimated uncertainty in liquid measurement is 20%. Comparisons of the radiometric water vapor retrievals with radiosonde data over extended periods show an rms agreement within 0.8 mm (Snider 1988). System output data were averaged for 1 min intervals during the FIRE IFO.

3. Shortwave cloud radiation parameterization

a. Background

Solar radiative transfer through stratocumulus clouds can be computed with reasonable accuracy given

a specification of the appropriate microphysical variables (optical thickness, single scattering albedo, asymmetry factor, and zenith angle). For our application, we wish to use measurements of a particular bulk cloud radiative transfer property (transmission coefficient) to deduce the integrated liquid water content and the albedo (solar reflection coefficient) of the overlying cloud. Thus, we are inverting the normal order of specified and computed parameters. Because the mathematical structure of the radiative equation is not very amenable to analytical inversion, we will use a conventional radiative transfer model for plane parallel clouds and iterate the microphysical variables until the computation yields the measured value of transmission coefficient. To streamline this process, we have chosen to use a radiative transfer parameterization (Stephens 1978) rather than a rigorous multiband radiative transfer code, as the accuracy of the basic measurements and the uncertainties associated with some of the assumptions in the radiative transfer models do not justify the expenditure of massive quantities of computer time for our particular application. While we are sacrificing theoretical purity for computational convenience, we can be reassured by the fact that the Stephens parameterization has been fit to measurements from a variety of real clouds. At any rate, from a measurement of the cloud transmission coefficient and a specification of solar zenith angle, we obtain from the parameterization the optical thickness and the cloud albedo. This approach is similar to that used by Gautier et al. (1980) to deduce cloud transmission from satellite measurements of albedo. A second parameterization relating optical thickness to integrated liquid water is used to compute W. Because the Stephens model represents an average over many cloud types, the accuracy of this second parameterization is examined explicitly for the stratocumulus clouds that dominate our data.

b. *Shortwave parameterization*

Stephens (1978) has developed a simple parameterization of cloud albedo (Re), transmittance (Tr), and absorption (Ab) in terms of the cloud optical thickness (τ) and the zenith angle (θ). The parameterization is based on the two-stream, two-band approximation of Coakley and Chylek (1975). A look-up table of values for single scattering albedo (ω) and backscatter fraction (β) is given as a function of τ and $\mu = \cos\theta$. These values are based on results of sophisticated 10-layer, 15-band radiative transfer computations. The revised look-up table (Stephens et al. 1984) is used for the work presented here. It is important to realize that these parameters are tuned so that, when used in the equations below, they give the same transfer properties as the sophisticated model. Thus ω cannot be strictly interpreted as the actual single scattering albedo of the medium (which should not depend on zenith angle), but as a surrogate parameter that produces the proper values for transmission coefficient, etc. A two-band wavelength (λ) structure is used: A shorter wavelength region ($\lambda < 0.7$ μm) where absorption is neglected and a longer wavelength region ($\lambda > 0.7$ μm) where absorption is considered. Because some of the earlier papers contain typographical errors, we will give the equations of the model here.

(i) Non-absorbing, $\omega = 1$

$$\mathrm{Re} = \beta\tau/\lambda(1 + \beta\tau/\lambda) \tag{1a}$$

$$\mathrm{Tr} = 1 - \mathrm{Re} \tag{1b}$$

(ii) Absorbing, $\omega < 1$

$$\mathrm{Re} = (u^2 - 1)[\exp(\tau_{ef}) - \exp(-\tau_{ef})]/R \tag{2a}$$

$$\mathrm{Tr} = 4u/R \tag{2b}$$

$$\mathrm{Ab} = 1 - \mathrm{Re} - \mathrm{Tr} \tag{2c}$$

where

$$u^2 = (1 - \omega + 2\beta\omega)/(1 - \omega) \tag{3a}$$

$$\tau_{ef} = (\tau/\mu)[(1 - \omega)(1 - \omega + 2\beta\omega)]^{1/2} \tag{3b}$$

$$R = (u + 1)^2 \exp(\tau_{ef}) - (u - 1)^2 \exp(-\tau_{ef}). \tag{3c}$$

When the cloud is over a reflective surface characterized by a surface albedo, a, then the reflection (Re′) and transmission (Tr′) coefficients of the combined system, neglecting subcloud effects, are given by

$$\mathrm{Re}' = \mathrm{Re} + a\mathrm{Tr}^2/(1 - a\mathrm{Re}) \tag{4a}$$

$$\mathrm{Tr}' = \mathrm{Tr}(1 - a)/(1 - a\mathrm{Re}) \tag{4b}$$

where Re and Tr are obtained from (2). For the remainder of this paper we will use the terminology Tr and Re to describe the results after correction by (4). We have used $a = 0.06$ for the ocean (Payne 1972).

The optical thickness is related to the cloud integrated liquid water using a parameterization obtained from an ensemble of different clouds (Stephens 1978):

$$\log_{10}(\tau) = 0.2633 + 1.7095 \log_e[\log_{10}(W)], \quad \lambda < 0.7\ \mu\mathrm{m} \tag{5a}$$

$$\log_{10}(\tau) = 0.3492 + 1.6518 \log_e[\log_{10}(W)], \quad \lambda > 0.7\ \mu\mathrm{m}. \tag{5b}$$

Because the Stephens parameterization was developed to apply to some 15 cloud types, we decided to compare it to a model with microphysics specific to the marine stratocumulus, which we shall refer to as the DFBS (Davidson et al. 1984) model. The DFBS model is a 15-band, delta–Eddington radiative transfer model that assumes a linear liquid water profile in the cloud that is computed from the adiabatic assumption based on specification of the MBL mean potential temperature and total water mixing ratio. A lognormal cloud droplet distribution is used where the mode ra-

dius is determined from the liquid water concentration at each altitude assuming a constant number of cloud droplets per volume, N. Initially $N = 100$ cm^{-3} was used to be consistent with typical observations in marine stratocumulus (see Davidson et al. 1984). Figure 2 shows a comparison of optical thickness versus integrated liquid water for the two models for a stratocumulus with cloud top at 600 m and total water (liquid plus vapor) mixing ratio of 8 g kg^{-1}, conditions similar to those encountered during the FIRE IFO. Optical thickness was varied by changing the cloud thickness from 50 to 450 m. Except for small values of W, the Stephens parameterization [Eq. (5)] is typically a factor of 1.8 higher than the DFBS values. Most of this difference can be explained by the fact that the Stephens parameterization is based on clouds with nominally 300 droplets cm^{-3}. The two models agree better for smaller values of W where the particular cloud type used by Stephens had $N = 120$ cm^{-3}. Stephens also assumed a constant vertical distribution of liquid water whereas the DFBS model assumes a linear distribution, which has the effect of slightly increasing optical thickness (see below).

To understand the differences in the two models, let us examine the microphysical aspects of the relationship between optical thickness and integrated liquid water content. Consider the log-Gaussian droplet concentration distribution used in the DFBS model,

$$n(x) = dN/dx$$
$$= N/[(2\pi)^{1/2}\sigma_x] \exp[-(x - x_m)^2/2\sigma_x^2] \quad (6)$$

where $x = \ln(r)$, r denotes droplet radius, σ_x the width of the distribution in log-radius space, $x_m = \ln(r_m)$ denotes the number density mode radius, N the total number of droplets per unit volume, and $n(x)$ the number of droplets per log-radius increment per unit volume. The kth moment of this distribution is given by

$$\langle r^k \rangle = N^{-1} \int n(x)dx = r_m{}^k \exp(k^2\sigma_x{}^2/2) \quad (7)$$

At any level in cloud, we can compute the extinction coefficient, α, and a liquid water concentration (mass/volume), Q_1,

$$\alpha = 2\pi N\langle r^2 \rangle \quad (8a)$$
$$Q_1 = (4\pi/3)\rho_w N\langle r^3 \rangle \quad (8b)$$

where ρ_w is the density of liquid water and we have assumed a Mie scattering efficiency of 2.0 because typical cloud droplets are much larger than the dominant solar wavelengths. At any level in the cloud, the incremental contribution to the optical thickness and integrated liquid water content can be computed from α and Q_1 for some height interval, dz:

$$d\tau = \alpha dz \quad (9a)$$
$$dW = Q_1 dz. \quad (9b)$$

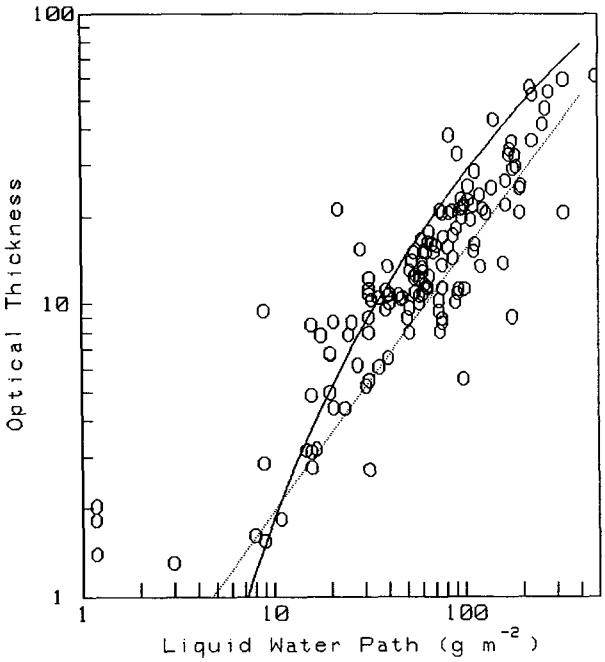

FIG. 2. Optical thickness (τ) versus integrated cloud liquid water (W) for the Stephens parameterization of Eq. (5a) (solid line), the DFBS calculations and Eq. (6) (dotted line), and measurements during the FIRE IFO (circles).

For a cloud with a uniform vertical distribution of liquid water and droplet number concentration and mode radius, Stephens (1978) has shown that $\tau = 3/2W/r_e$, where the effective radius $r_e = \langle r^3 \rangle / \langle r^2 \rangle$. Using (7), we can eliminate the particle radius parameter and write the optical thickness, τ_0, for a uniform cloud in terms of the cloud thickness, Δz,

$$\tau_0 = 2\pi[3/4\pi\rho_w]^{2/3} \exp(-\sigma_x{}^2) N^{1/3} W^{2/3} \Delta z^{1/3}. \quad (10)$$

Because the cloud is uniform, $W = Q_1 \Delta z$.

For stratocumulus clouds, we assume that the N and σ_x are constant in the cloud, but the liquid water concentration varies linearly from cloud bottom (z_b) to cloud top (z_i):

$$Q_1 = \Gamma(z - z_b); \quad z_b < z < z_i. \quad (11)$$

The coefficient Γ is approximately 0.0002 times the mixed-layer total water concentration (see Albrecht et al. 1990). Note that (8b) and (11) determine the droplet mode radius as a function of height within the cloud. Integration of the optical thickness and liquid water equations yields $W = \Gamma \Delta z^2/2$ and $\tau = (3/5)2^{2/3}\tau_0$. The latter result implies that a cloud with a linearly increasing liquid water concentration has abut 5% less total optical thickness than a uniform cloud of the same geometrical thickness and integrated liquid water content. Finally, we can eliminate the physical thickness of the cloud to obtain

$$\tau = (3/5)2^{5/6}[3/4\pi\rho_w]^{2/3}$$
$$\times \exp(-\sigma_x{}^2)\Gamma^{-1/6} N^{1/3} W^{5/6} \quad (12)$$

which falls very close to the DFBS model curve in Fig. 2. The DFBS model computes Mie scattering efficiencies and includes liquid water and vapor absorption effects, so it yields slightly higher values for τ, but this equation expresses the basic sensitivity to microphysical parameters of the DFBS τ versus W relationship.

Because the DFBS model has been optimized for marine stratocumulus, we expect it to describe the clouds at SNI better than the Stephens parameterization. We shall see in the next section that the clouds encountered at SNI during the FIRE IFO exhibited optical thicknesses typically between the two models. A best fit to the IFO data is

$$\log_{10}(\tau) = -0.48 + 0.88 \log_{10}(W) \qquad (13)$$

which is about 30% above the DFBS model. If we use (13) to specify the optical thickness, then the DFBS and Stephens radiative transfer parameterizations give essentially the same transmission coefficients (Fig. 3). Using this slightly modified form of the Stephens model, a nomogram can be constructed that gives contours of transmittance versus zenith angle and integrated liquid water path (Fig. 4) for stratocumulus clouds.

c. *The shortwave algorithm*

The computations are performed in the following manner. The basic data consist of a time series of one-hour averages of solar irradiance. The time series is broken into two-week segments, and a "clear-sky" irradiance is established for each hour of the daytime in that two-week segment. This is done either by selecting an obvious clear day in the segment or using maximum solar irradiances obtained from several partly cloudy days in the segment. A "clear-sky" irradiance is then computed for each daytime hour for each day during the entire eight-month period by interpolating between these selected reference days. Obviously a single clear-sky value cannot be used for the entire eight-month period because of seasonal variations in solar declination. This approach also has the advantage that, at least to first order, seasonal variations in the above-cloud transmission coefficient can be removed. Short term variations in the above-cloud transmission coefficient will be the major source of error of this approach, particularly if there are systematic differences between the cloud and no-cloud circumstances. We have made no attempt to assess this source of uncertainty. The cloud transmission coefficient is then calculated as the ratio of the measured solar irradiance to the clear-sky irradiance for each hour of the day. The zenith angle for that hour of the day is computed from the Julian date and the latitude and longitude of the site. An initial value for W is estimated, and a solar transmission coefficient is computed as described above. The value for W is then adjusted until the computed transmission coefficient agrees (within some specified limit) with the measured value. This yields values of W and Re that are consistent with the measured cloud transmission coefficient.

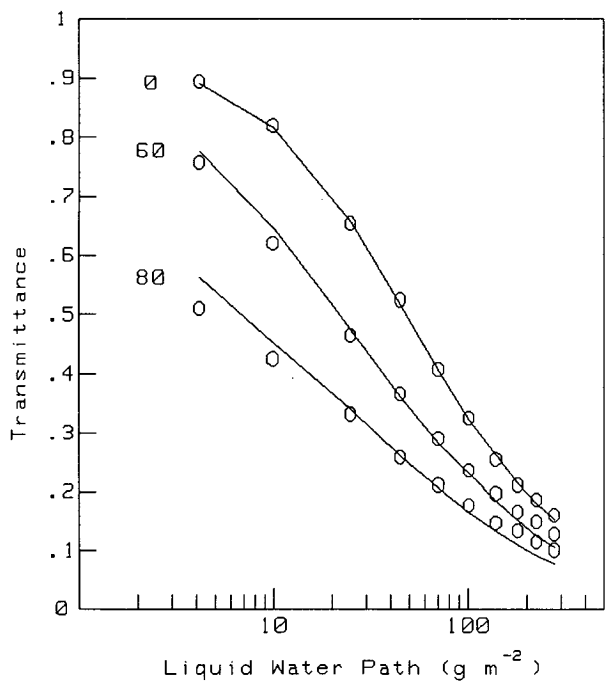

FIG. 3. Comparison of transmittance (Tr) versus integrated cloud liquid water (W) at zenith angles of 0, 60, and 80 degrees for the Stephens (circles) and DFBS (line) models.

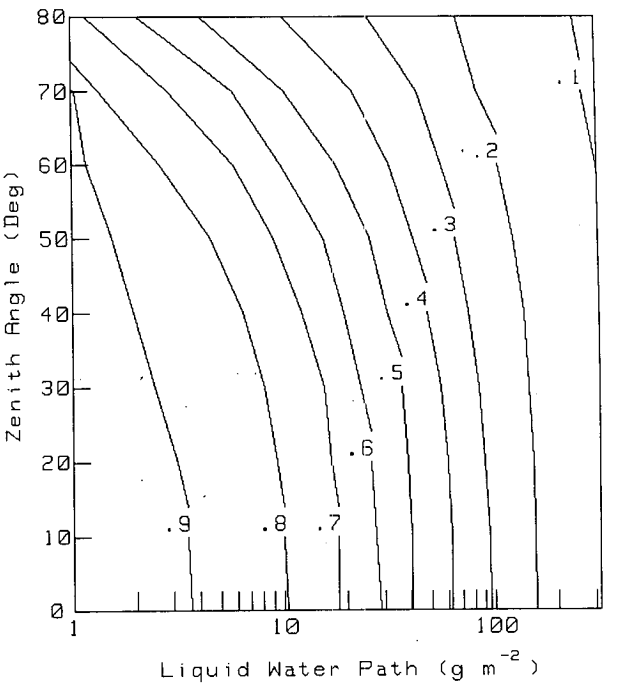

FIG. 4. Contours of transmittance (Tr) as a function of solar zenith angle (θ) and integrated cloud liquid water (W) from the modified Stephens parameterization.

4. Evaluation of the shortwave parameterization for W and Re

The intensive field program held at SNI in 1987 yielded a short period of colocated measurements of W from the NOAA radiometer (1 July to 19 July). Only one day (4 July) in this period was completely clear; most days had total cloud cover (see the cloud fraction depiction in section 6). In comparing microwave radiometer and solar-derived values for W, low incidence angles ($\mu < 0.4$) were not used because of the potential for large errors. For the same reason, transmittances greater than 0.9 were not considered. The comparison for relationship of τ to W is shown in Fig. 2.

The values of τ estimated from the measured transmittances are on average 30% higher than the values derived from DFBS model and about 50% lower than the values derived from the original Stephens parameterization. A log–log linear regression of τ versus W data from the IFO yields a correlation coefficient of 0.87. The rms scatter about the regression line represents about 35% variability in the value of W (or τ since they are roughly proportional). Some of this scatter is due to differences in sampling geometry, since the pyranometer has a hemispherical field of view and the radiometer has a narrow field of view. These differences in field of view are somewhat moderated by averaging for one hour. Another source of error is the use of an interpolated clear sky irradiance based on a single sample for the entire 17-day period. As we mentioned earlier, we expect the SNI stratocumulus data to fall significantly below the Stephens parameterization because clouds in the California region typically have much fewer drops than those used by Stephens. The 30% systematic underestimate of τ by the DFBS model is a more puzzling issue, since it has been optimized for these conditions. The accuracy of the liquid water measurement by the NOAA radiometer is believed to be better than 20%. While a 30% systematic error of integrated liquid water by the radiometer is not totally out of the question, a comparison against values calculated on the basis of the adiabatic assumption (Albrecht et al. 1990) suggests that this system is even more accurate than the 20% figure.

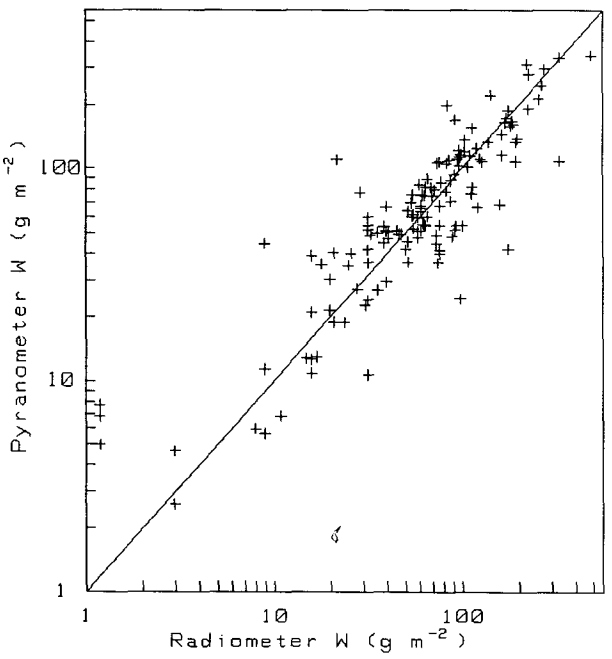

FIG. 5. Integrated cloud liquid water (W): as computed from solar transmittance (vertical axis) versus the NOAA radiometer measurements (horizontal axis).

In pondering the disagreement between the two measurements, we believe the best evidence suggests that the microwave radiometer values for W are quite accurate. This leads us to ask why values of τ computed from W using the DFBS model might be too small (conversely, use of the DFBS parameterization to compute W from measured values of τ would lead to overestimates of W). One possibility is nonlinear effects entering the relationship of mean integrated liquid water to mean transmission coefficient. An obvious second possibility lies in the cloud droplet microphysics assumptions or the computation of τ within the DFBS model.

Coakely (1988, personal communication) has suggested that the nonlinear relation between integrated liquid water and transmission (or albedo) of clouds can lead to a bias in mean liquid water deduced from a mean transmission coefficient. To see this, let us perform a Taylor expansion of transmission about the mean value of W and then average,

$$\langle W \rangle = W(\langle \mathrm{Tr} \rangle)[1 + S(\sigma_w/\langle W \rangle)^2] \quad (14)$$

where quantities enclosed by the brackets, $\langle\ \rangle$, have been averaged. The dimensionless nonlinear sensitivity coefficient, S, is given by

$$S = -(1/2)[\partial^2 \mathrm{Tr}/\partial(\ln(W))^2]/[\partial \mathrm{Tr}/\partial(\ln(W))]. \quad (15)$$

We can use the Stephens parameterization to evaluate (15) by numerically computing finite-difference first and second derivatives at various values of zenith angle and mean integrated liquid water content. As defined here, S, is positive over the range of W values of interest here (becoming negative at very small values of W), so small-scale cloud variability tends to cause us to underestimate W from the mean transmission coefficient. From the high speed (1 min) time series of W from the microwave radiometer we have computed σ_w on a one-hour time scale. A typical value for σ_w/W is on the order of 0.25. Larger values are observed for smaller W, but this is compensated by the decrease in S. Using a value of $S = 1.2$ for $W \approx 50$ g m^{-2}, we find that nonlinear effects reduce the pyranometer es-

timates of W by about 7.5%. This effect makes our disagreement worse but is essentially negligible.

We can use (12) to examine the microphysical factors that might explain differences in the DFBS model and the FIRE IFO data. Note that subadiabatic liquid water content (smaller Γ), narrower droplet distributions (smaller σ_x), and more cloud droplets per unit volume (larger N) would improve the agreement. However, the Γ dependence is so weak that a realistic reduction (say 20%) would not be observable. Also, reduction of the current value of σ_x from 0.34 to 0 (i.e., single droplet size) would only increase τ by 12%. A doubling of the cloud droplet number concentration would account for the disagreement. Preliminary evaluations of FIRE IFO cloud droplet concentrations from aircraft have found N typically between 50 and 100 cm^{-3}, although most of this data was taken much farther from the coast than SNI. Because we expect greater aerosol concentrations nearer the coast (with higher cloud droplet concentrations and higher cloud albedos), we cannot rule out the possibility that locally large values of N explain the difference in the measurements and the DFBS model. This point will become more clear when measurements of cloud droplet concentrations made at SNI by tethered balloon-borne sensors become available at some later date.

Clearly, based on the above assessment, nonlinear effects cannot account for the discrepancy we have observed. The major fraction must be due to differences in cloud droplet concentration, a bias in our parameterization, a systematic error in the microwave radiometer values, or some other effect that we have overlooked. For the purposes of constructing our climatology, we will take the utilitarian points of view and use the best fit of the observed values of τ and W for the SNI IFO period as given in (13). The resultant comparison for radiometer and pyranometer-derived values for W is given in Fig. 5. We will assume that this adjustment is applicable over the March to October period.

5. Longwave parameterization for cloud fraction

a. Background

The definition of cloud fraction is often confused by the concepts of scale. A 24-hour period of broken clouds at a given location may yield the same average cloud cover as 12 hours of solid stratus followed by 12 hours of clear skies, but on a larger scale the stratus may be considered to be part of a broken cloud field. For our purposes, we will consider cloud fraction, f, to be the fraction of time in one hour that a narrow field of view instrument in a zenith pointing mode (i.e., a lidar ceilometer) detects the presence of a cloud overhead. During the FIRE IFO this parameter almost always had a value of zero or one (Fig. 6), which is typical for stratus clouds. Later we will compute daily or monthly averages that represent the average cloud coverage over that period without mentioning the "fractional" structure of the clouds. In principle, such information is still contained in a time series of ceilometer data, but our pyrgeometer is a broad field of view instrument and is more limited in defining small-scale structure. We will continue to use the conventional term "fractional cloudiness," but the reader is alerted to the fact that we are using it in a time-averaged sense.

Because it is well known that the downward longwave radiative flux received at the surface is substantially greater (by roughly 100 W m^{-2}) in the presence of stratocumulus clouds versus clear skies, we developed an algorithm to estimate f from the pyrgeometer time series. We considered two approaches: (1) compute f by comparing the measured downward longwave irradiance, L_m, to anticipated values for clear, L_0, and stratocumulus conditions, L_s, and (2) compute f by comparing the standard deviation of downward longwave, σ_1, to L_0 and L_s. The values for L_0 and L_s are obtained from standard bulk models of downward longwave irradiance. In the end we chose method (2) because it is significantly less sensitive to the details of our determination of L_0 and L_s at the extremes (i.e., $f = 0$ or 1.0). Thus, the particular algorithm we have used is better at determining cloud versus no cloud than providing estimates of fractional cloudiness on one-hour time scales. As we will see below, this could be improved significantly with more accurate parameterization of downward longwave radiation.

b. The longwave parameterization

A variety of simple bulk models are available to estimate L_0 for near surface meteorological data (see reviews by Simpson and Paulson 1979; Siegel and Dickey 1986). We have chosen Brunt's (1932) equation

$$L_0 = \epsilon_a \sigma T_a^4 \tag{16}$$

where T_a is the near surface air temperature, σ the Stefan–Boltzmann constant, and ϵ_a the effective clear-sky emissivity. The effective clear-sky emissivity is given by

$$\epsilon_a = 0.60 + 0.04(e_a)^{1/2} \tag{17}$$

where e_a is the partial pressure of ambient water vapor near the surface (expressed in millibars). In the presence of stratocumulus clouds, we use a modification of (16)

$$L_s = L_0 + (1 - \epsilon_a)\sigma T_b^4, \tag{18}$$

where T_b is the estimated cloud base temperature, which is computed from the lifting condensation level, $z_b = (\gamma_a - \gamma_d)(T_a - T_d)$,

$$T_b = T_a + \gamma_a z_b. \tag{19}$$

Here T_d is the dewpoint temperature (computed from e_a), γ_a is the adiabatic lapse rate of temperature (0.0098 K m^{-1}), and γ_d the adiabatic lapse rate of dewpoint

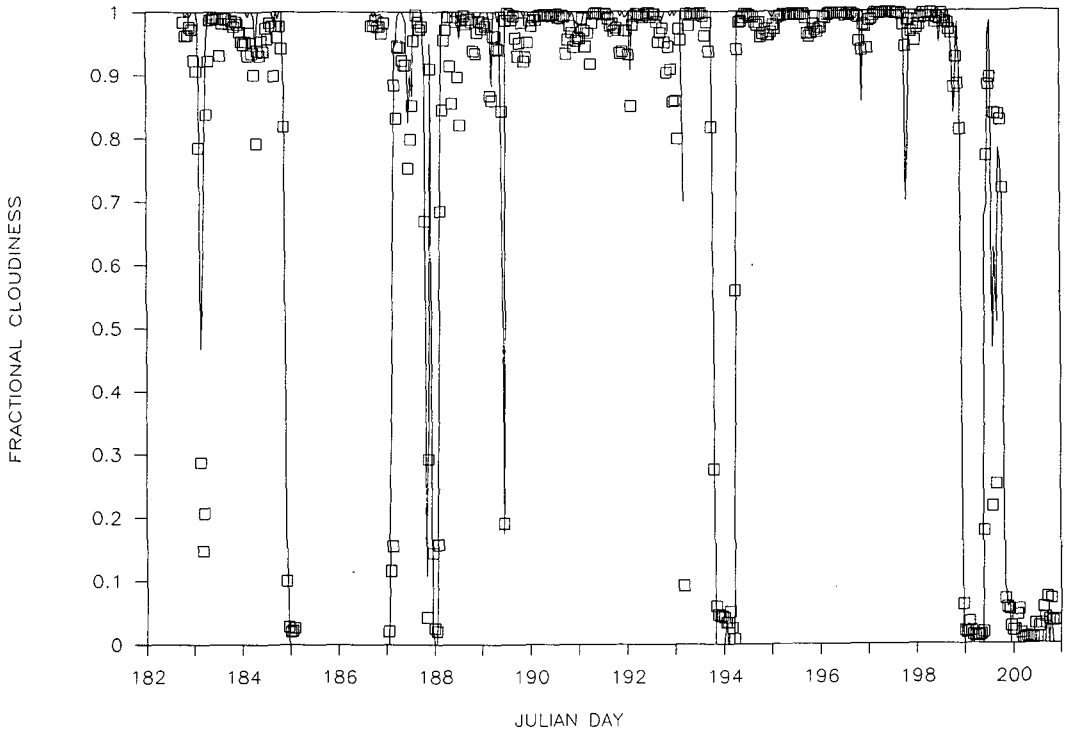

FIG. 6. Time series (one-hour time scale) of the fractional cloudiness, f, for the FIRE IFO period. The solid line is from the lidar ceilometer and the square boxes are values computed from the standard deviation of longwave irradiance using (23) with m = 1.0.

temperature (0.0018 K m^{-1}) under well-mixed conditions.

If the formulae for L_0 and L_s were accurate, we would postulate that a reasonable estimate of the cloud fraction would be given by

$$f = (L_m - L_0)\Delta, \tag{20}$$

where $\Delta = L_s - L_0$. However, these simple models do not incorporate enough information to describe a large part of the variability of L_0 and L_s (Siegel and Dickey 1986). In an effort to obtain a more reasonable estimate, we decided to use the variance of the measured radiation, σ_1^2. Obviously if the sky is completely clear or totally cloud covered, this variance will be very small. We postulate that broken clouds drifting overhead will lead to substantial short-term variability in L_m that is reflected in σ_1. Because of the broad field of view of the pyrgeometer, the variance will not provide a complete description of the variability. For instance, we can imagine a field of small broken clouds moving slowly or simply so small that the pyrgeometer field of view averages most of the variations even for short periods. To develop our algorithm, we will start with an idealized view of broken clouds which we represent as a "rectangular wave" of period T. For a fraction, f, of T we let the downward longwave irradiance be given by $L = L_0 + \Delta$; for the remaining fraction, $(1 - f)$, of T we let $L = L_0$. Thus, the average value of L measured in the period is

$$\langle L \rangle = L_m = L_0 + f\Delta \tag{21}$$

which forms the basis of (20). The total variance of L is given by

$$\sigma_1^2 = \langle (L - \langle L \rangle)^2 \rangle = f(1 - f)\Delta^2, \tag{22}$$

where we note that $(L - \langle L \rangle)^2$ has the value $\Delta^2(1 - f)^2$ over the interval of length f and the value $\Delta^2 f^2$ over the interval $(1 - f)$. Thus, (22) results from an interval-length-weighted average of these values of $(L - \langle L \rangle)^2$.

We can express the solution to (22) as

$$f = \{1 \pm [1 - 4(\sigma_1/\Delta)^m]^{1/2}\}/2, \tag{23}$$

where for the quadratic form of (22) we have $m = 2$. We have left this exponent as an adjustable parameter because of the field-of-view sampling problem discussed above. We will see in section 6 that $m = 1$ gives a better fit to the FIRE IFO data. Because (23) is double valued, we need a method to select which sign (+ or −) is appropriate. Here we use the measured mean irradiance: If $L_m < L_0 + \Delta/2$, then we use the negative sign in (23). This implies that our algorithm will be most inaccurate when it yields $f \approx 0.5$, where the result is critically dependent on the accuracy of (16), (17), and (18).

Thin clouds will also cause a problem with this approach. Clouds thinner than about 100 m will exhibit reduced values for L_m and σ_1 because their longwave emissivity is less than 1.0. For example, solid but very thin clouds (which have very small σ_1) are classified as clear ($f = 0$) when their emissivity is less than 0.5 (L_m is less than $L_0+\Delta/2$). For broken clouds, the effects are complicated. Slightly broken, thin clouds have their value of f overestimated (because σ_1 is reduced) unless L_m is less than $L_0+\Delta/2$, in which case f is underestimated. While such conditions were essentially unobserved during the FIRE IFO, the reader is cautioned that this represents another source of uncertainty in our results.

6. Evaluating the longwave parameterization for f

The lidar ceilometer provides two measurements, cloud base height, z_b, and (when averaged) cloud fraction. The ceilometer-derived cloud fraction for the FIRE IFO is shown in Fig. 6. A comparison of ceilometer and surface meteorological estimates of z_b is shown in Fig. 7. Note that (19) tends to underestimate z_b. This is partly due to violation of the well-mixed assumption (Davidson et al. 1984) and to the tendency of our relative humidity sensors to overestimate the RH after lengthy exposure to the marine environment. This latter effect is apparent in the periodic fog events that are common at SNI. Under foggy conditions the RH should be near 100%, but by the end of the eight-month period the RH sensor values were occasionally exceeding 110%. The error in z_b indicated in Fig. 7 represents an overestimate of L_s of less than 5 W m^{-2}. Because this is relatively small compared to the uncertainty of L_s, we will ignore it for our purposes.

The mean and standard deviation of downward longwave irradiance for the IFO period are shown in Fig. 8. We have chosen a display measured longwave irradiance in the form $(L_m - L_0)/\Delta$ so that the values on the horizontal axis represent f deduced from L_m via (20). The vertical axis is σ_1/Δ. The data points from a pattern similar to the arches shown by Coakley and Bretherton (1982). The cluster of points on the lower right of the graph represent solid cloud cover. Clear skies should appear as a cluster of points in the lower left corner. If (22) were exactly obeyed and our expressions for L_0 and L_s were accurate, then the points would lie on the upper solid lines, which is computed using $m = 2$. Clearly, the measured standard deviations of longwave irradiance are much smaller than expected theoretically and lie much closer to the lower solid line in the figure (corresponding to $m = 1$). This is probably due to the averaging affects of the wide field of view of the pyrgeometer. Note that a number of points with very low variance fall well away from the edges of the graph, particularly on the left side of the graph. This is an indication of the inability of (16) to predict L_0 correctly. The relatively tightly packed clump of points in the lower right-hand corner of the graph implies that the parameterization for L_s is quite good. This makes sense because L_s is dominated by the cloud base temperature, which cannot be greatly different from the near surface air temperature in the stratocumulus regime.

Ceilometer measurements of f (which are considered to be the standard) were compared with f computed from (20) and from (23) for various of m. We found that (23) with a value of $m = 1$ gives the best results (see Fig. 9). The mean value of f for these data is 0.80 for the pyrgeometer algorithm and 0.83 for the

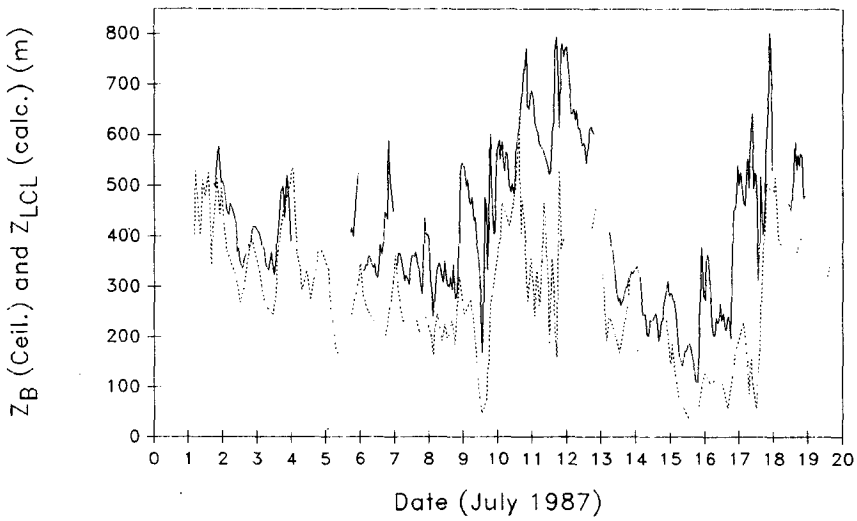

FIG. 7. Time series of cloud base height during the FIRE IFO period. The solid line is directly determined from the lidar ceilometer; the dashed line is the lifting condensation level computed from near surface measurements of air temperature and dewpoint temperature.

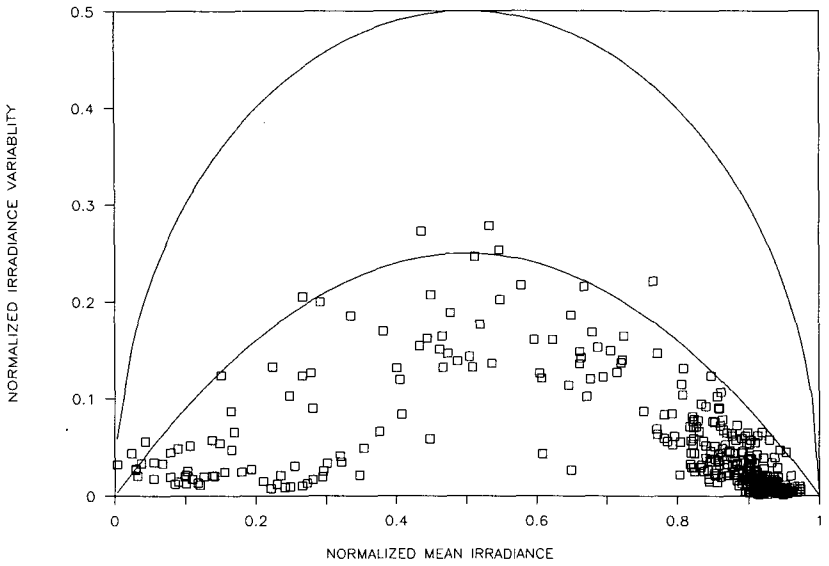

FIG. 8. Standard deviation (one-hour time scale) of longwave irradiance (σ_1) normalized by $\Delta = L_s - L_0$ (the expected difference in cloudy and clear irradiances) versus the deviation of the mean longwave from the expected clear sky value (also normalized by Δ) for the FIRE IFO period. The latter parameter is the mean-irradiance estimate of the fractional cloudiness. The upper solid line represents the theoretical behavior expressed by (23) with $m = 2$. The lower solid line is for $m = 1$.

ceilometer. A linear regression yields a slope very near one with a correlation coefficient of 0.977. The rms scatter about the regression line represents about 0.074 uncertainty in a particular value of f.

The IFO time series for f using (23) have been included in Fig. 6. Finally, a graph of estimated pyrgeometer values of f plotted against simultaneous values of the solar transmittance of the clouds is given in Fig. 10. This graph displays the bimodal structure of the cloudiness. The upper branch represents stratocumulus clouds with decreasing thickness and occasional holes in the cloud as solar transmittance increases. The lower branch represents basically clear skies with a few cases of reduced transmittance due to haze or a few isolated

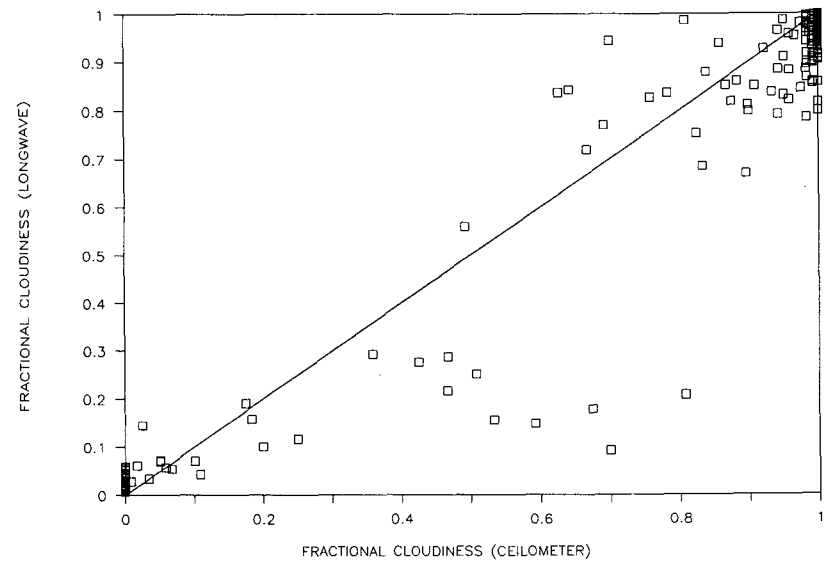

FIG. 9. Comparison of fractional cloudiness as directly measured with the lidar ceilometer (horizontal axis) versus computations from the standard deviation of longwave irradiance [via Eq. (23)] for the FIRE IFO period. The straight line represents perfect agreement.

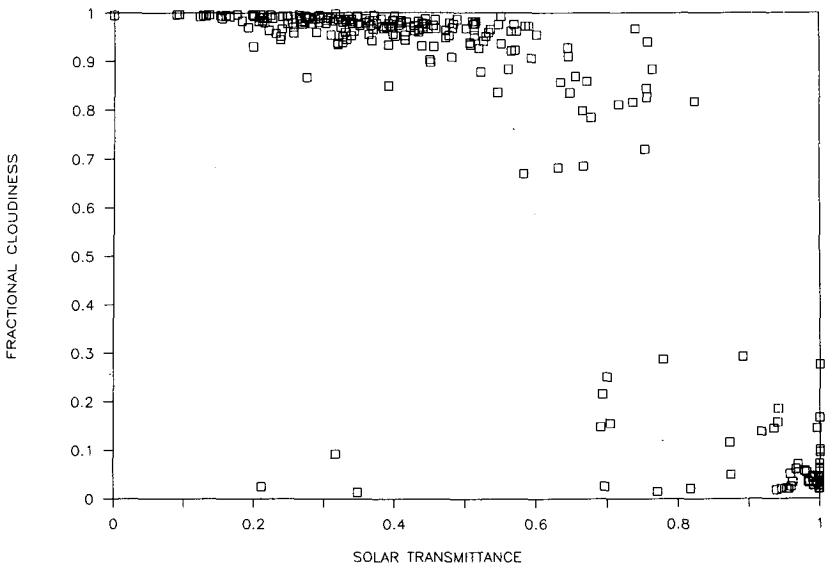

FIG. 10. Fractional cloudiness, f, determined from the longwave irradiance versus solar transmittance, Tr, determined from the shortwave irradiance. The points in the upper part of the graph are believed to represent stratocumulus conditions; the lower right corner represents clear skies; the lower points ($f \approx 0$) with reduced transmittance represent haze or very small optically thick clouds. No cirrus was observed during the FIRE IFO.

clouds that happen to obscure the sun during the period.

7. Eight-month statistics

The system at SNI provided a nearly continuous record of 30-minute averages of the data from Julian day 50 to 285. One period (day 142 to 154) was lost due to an extended power outage. For example, the time series of solar irradiance for the entire period is shown in Fig. 11. At this graphical resolution, each day appears as a spike whose top is essentially the noon maximum. The summer heavy stratocumulus season is apparent as repeatedly depressed noon maxima (for example, between day 120 to 200). This is also apparent in the time series of weekly average mean cloud

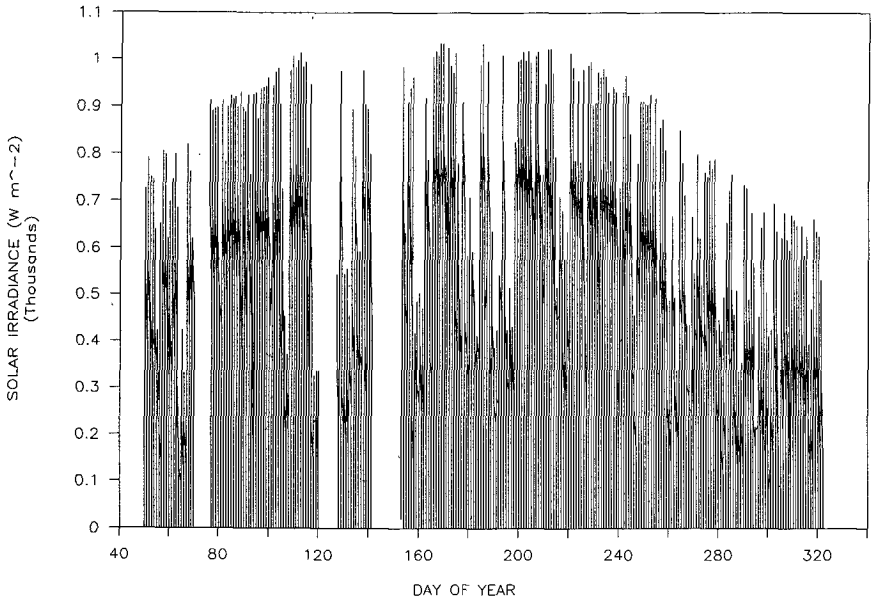

FIG. 11. Time series of solar irradiance for the entire eight-month data period.

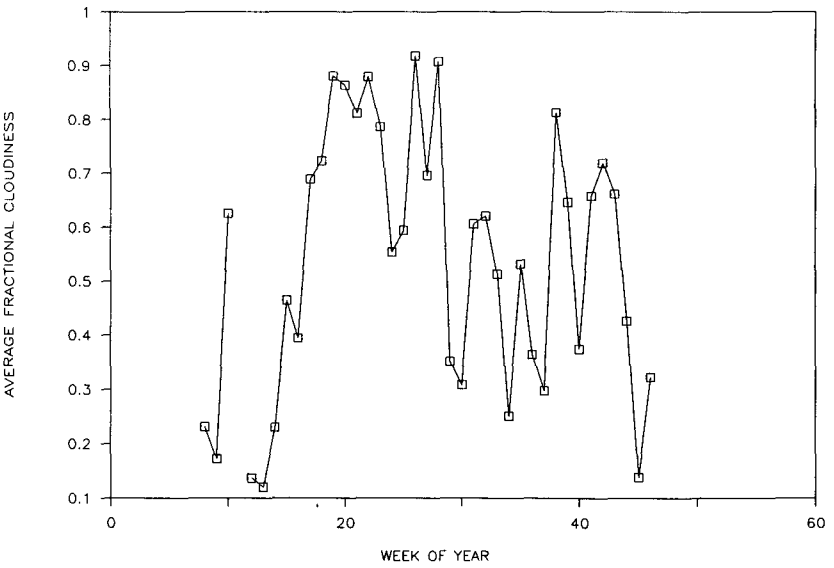

FIG. 12. Time series of weekly averaged fractional cloud cover, computed from the longwave irradiance, for the eight-month data period. The stratocumulus season is evident as the high values of f in the April to September period.

cover (Fig. 12). The stratocumulus season set in about week 18 and ended about week 42 with a few intermediate weeks of respite.

A variety of statistics have been computed from this database. Frequency distributions have been computed for lifting condensation level estimates of cloud base height (Fig. 13a), albedo (Fig. 13b), integrated cloud liquid water (Fig. 13c), and cloud fraction (Fig. 13d). Because the sun is only up during the day, statistics compiled from the pyranometer data are biased because they represent daytime periods. Also, the albedo and W statistics are only computed when clouds are present (as indicated by a transmittance < 0.9). In other words, clear sky conditions are not considered in these particular statistics. Strong marine influence is apparent in Fig. 13a where the lifting condensation level is predominantly below 600 m. Negative values for lifting condensation level indicate that the hygrometer is reading (erroneously) over 100% relative humidity. Figures 13b and 13c imply that the typical daytime stratocumulus at SNI has an integrated liquid water content of about 75 g m^{-2} and an albedo of 0.55. Cloud base height and cloud fraction can be analyzed by a joint frequency distribution in order to classify the cloud regime in a slightly different manner than in Fig. 10. This joint frequency distribution is shown in Fig. 14. The stratocumulus regime occupies the lower right-hand portion of the domain; basically clear conditions are on the left side of the domain. The lack of occurrences of conditions in the center of the domain suggest that partial low cloud cover, at least on the time/space scales relevant for these data, is quite rare at SNI for the seasonal period of our analysis. Notice also that there are a surprising number of occurrences of clear conditions with rather low cloud base heights. This could be due to a very low marine inversion or to substantial gradients of potential temperature and water vapor mixing ratio in the MBL (i.e., violations of the well-mixed hypothesis used to compute z_b from near surface data).

Based on model studies (e.g., Fravalo et al. 1981; Davidson et al. 1984) stratocumulus clouds are expected to have moderate diurnal variability, primarily due to raising of z_b by solar warming of the MBL through cloud radiative absorption. Raising z_b will reduce the vertical thickness, integrated liquid water content, optical thickness, and albedo of the cloud (assuming the cloud top height does not change). Satellite observations (Minnis and Harrison 1984; Minnis et al. 1987) have verified this expectation for cloud amount and albedo. The FIRE IFO data indicated substantial diurnal variations in W (Albrecht et al. 1989) as measured by the microwave radiometer. Cloud fraction and cloud thickness also show a measurable diurnal variation. An average diurnal cycle of cloud fraction for the three summer months (Fig. 15) shows a substantial modulation of the clouds, presumably caused by the mechanism discussed above. We have included on this figure the diurnal cycle observed during the IFO so that the excellent comparison between the ceilometer and longwave algorithm can be seen. Despite the limitations of the solar data, we have computed average diurnal cycles for albedo (Fig. 16a) and W (Fig. 16b). To broaden the part of the diurnal cycle covered, we have relaxed the restriction on solar zenith angle to permit computations for $\mu > 0.1$. The

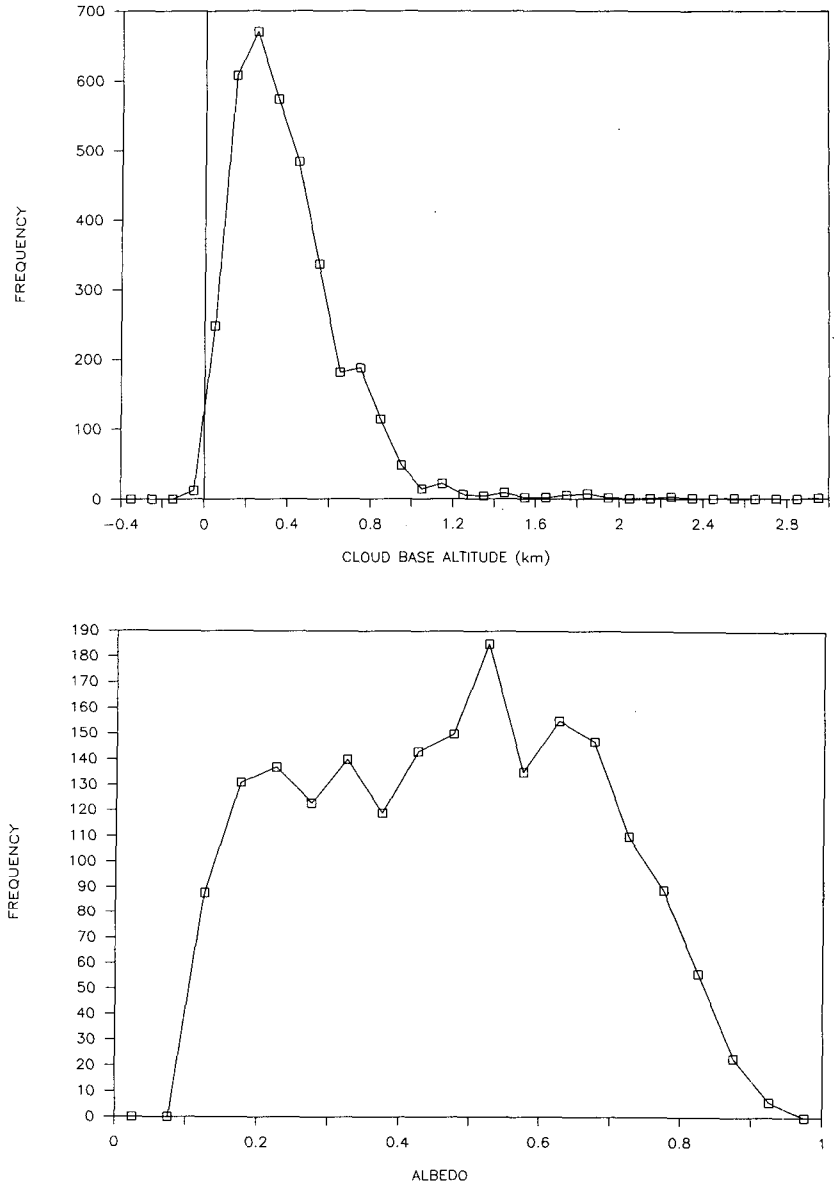

FIG. 13. Frequency distributions of the one-hour data, computed using the methods described in the text, for the eight-month period: (a) Cloud base height, (b) cloud albedo, (c) integrated cloud liquid water, and (d) fractional cloudiness. Note that (b) and (c) distributions are for daytime only.

fact that the mean values of W appear to increase from very low values for the first three hours after sunrise (Fig. 16b) is evidence that our algorithm is not reliable if $\mu < 0.4$. Only the seven hours centered about local noon can be considered usable (this also holds for the albedo calculation). Again, recall the clear sky conditions are not included in the W and albedo statistics, which then represent the diurnal changes of clouds when they are present but do not take into account the possibility of clouds being completely cleared in the course of a diurnal cycle. Also included on this figure is the average diurnal cycle observed during the IFO for both the microwave radiometer and the pyranometer derived values.

8. Discussion

A great deal of this paper has been devoted to describing and verifying simple methods of processing data obtained from standard and reliable radiative flux and bulk meteorological instruments. Such devices are capable of continuous operation in the marine envi-

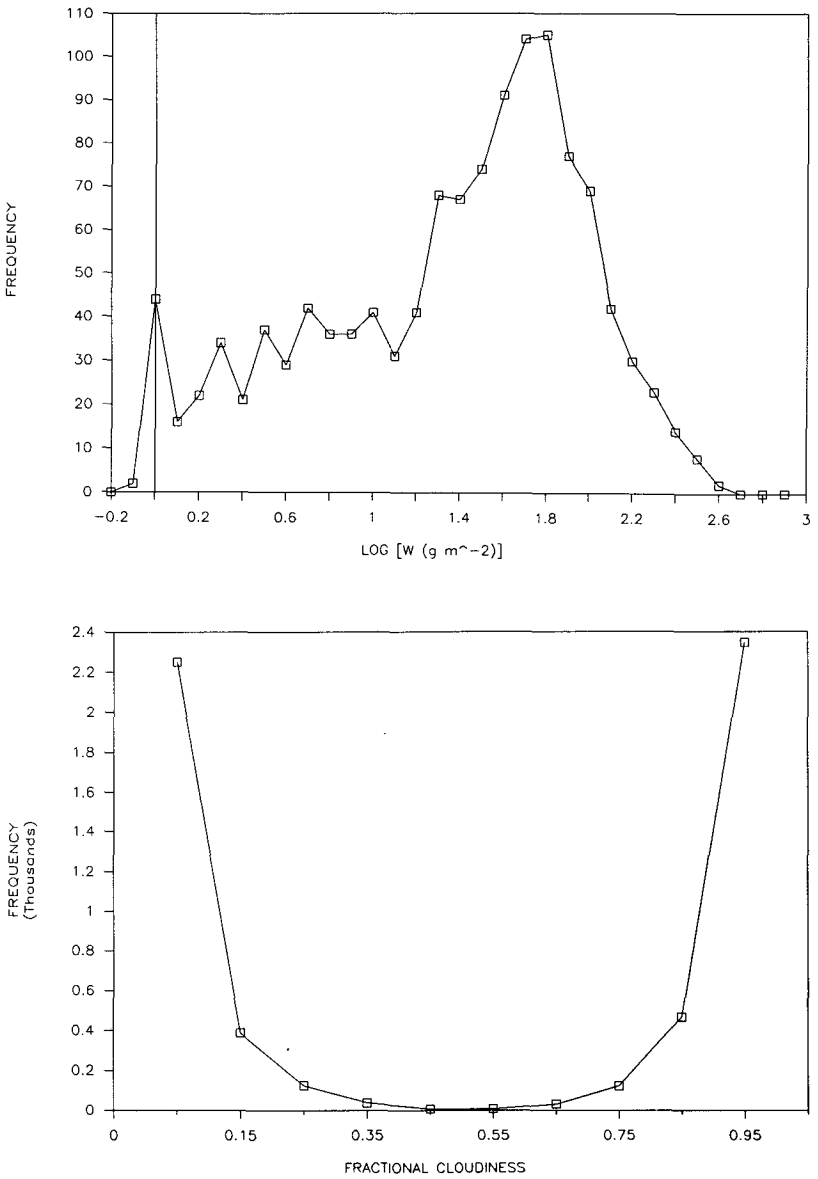

FIG. 13. (*Continued*)

ronment for many months with only occasional cleaning of the domes. Their primary function has historically been to provide measurements of the surface energy budget. However, using relatively simple models for downward longwave and shortwave irradiances, we have been able to deduce cloud fraction, integrated liquid water content, and albedo from such data. Combinations of the data can also be informative. For example, a joint distribution of cloud fraction and solar transmittance clearly differentiates between stratocumulus and mostly clear regimes. Following this approach, perhaps augmented with additional sensors, fairly sophisticated statistics could be obtained on fundamental cloud parameters.

Comparisons against more direct measurements made during the FIRE intensive field operation have shown these algorithms to be quite powerful, although there is still room for improvement. Some questions still remain to be answered. For example, the relationship between τ and W observed at SNI was not in agreement with the DFBS model. A variety of explanations were considered including nonlinear averaging effects, the number concentrations of cloud droplets, and the microwave calibration. For the purposes of using the algorithm for the entire database, we simply forced it to agree with the microwave system by using a best fit to the IFO data. This is equivalent to multiplying the DFBS computed values of τ by 1.3. This

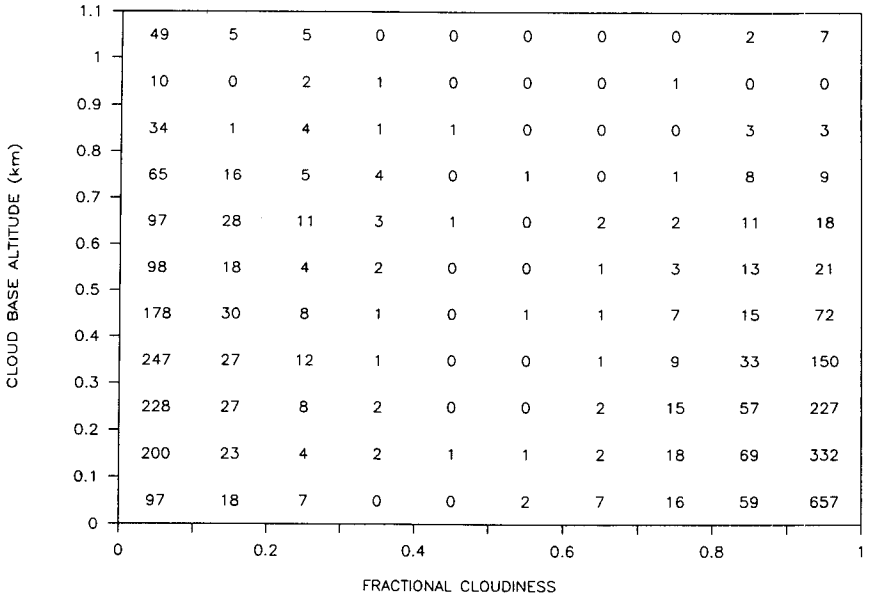

FIG. 14. Joint frequency distribution (unsmoothed) for cloud base height (estimated from lifting condensation level) and cloud fraction [estimated via Eq. (23)]. Stratocumulus cloud conditions occur on the right side of the graph (high cloud fraction) and are characterized by cloud bases typically less than 400 m.

issue may be resolved as more of the FIRE IFO data become available.

It is also important to avoid overselling this approach. The algorithms developed here are most appropriate for marine stratocumulus. They have been verified against a single 18-day dataset. The cloud fraction algorithm we have used is most effective as a cloud versus noncloud indicator and obviously will work best with very low cloud base and solid clouds of at least 100 m thickness. The ceilometer is a more appropriate device for this purpose (it also yields more accurate cloud base height than the lifting condensation level computation), but it costs an order of magnitude more than the pyrgeometer. The pyranometer algorithm provides important information on cloud microphysical and radiative transfer properties, but only during

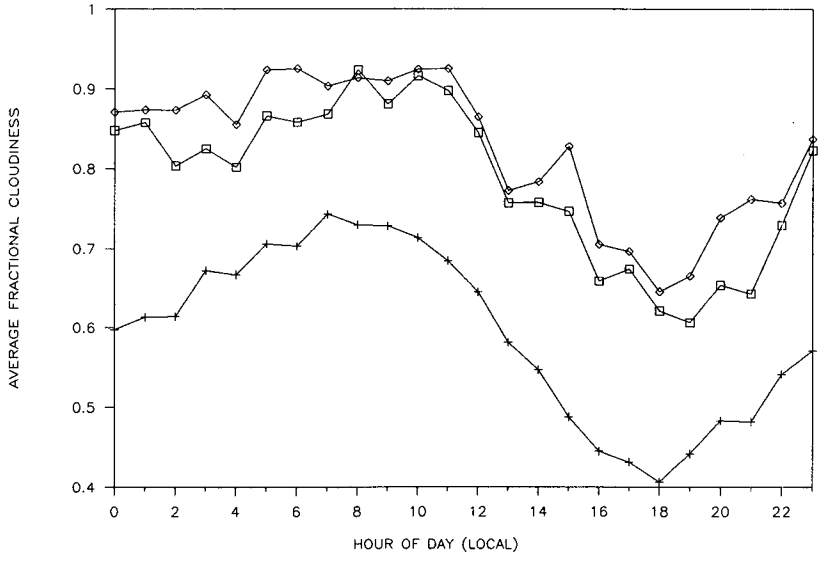

FIG. 15. Average diurnal variation (using local time) for fractional cloudiness, derived from the longwave irradiance, during the three summer months (plus symbol), and during the IFO period using the ceilometer (diamond symbol) and the longwave irradiance (square symbol).

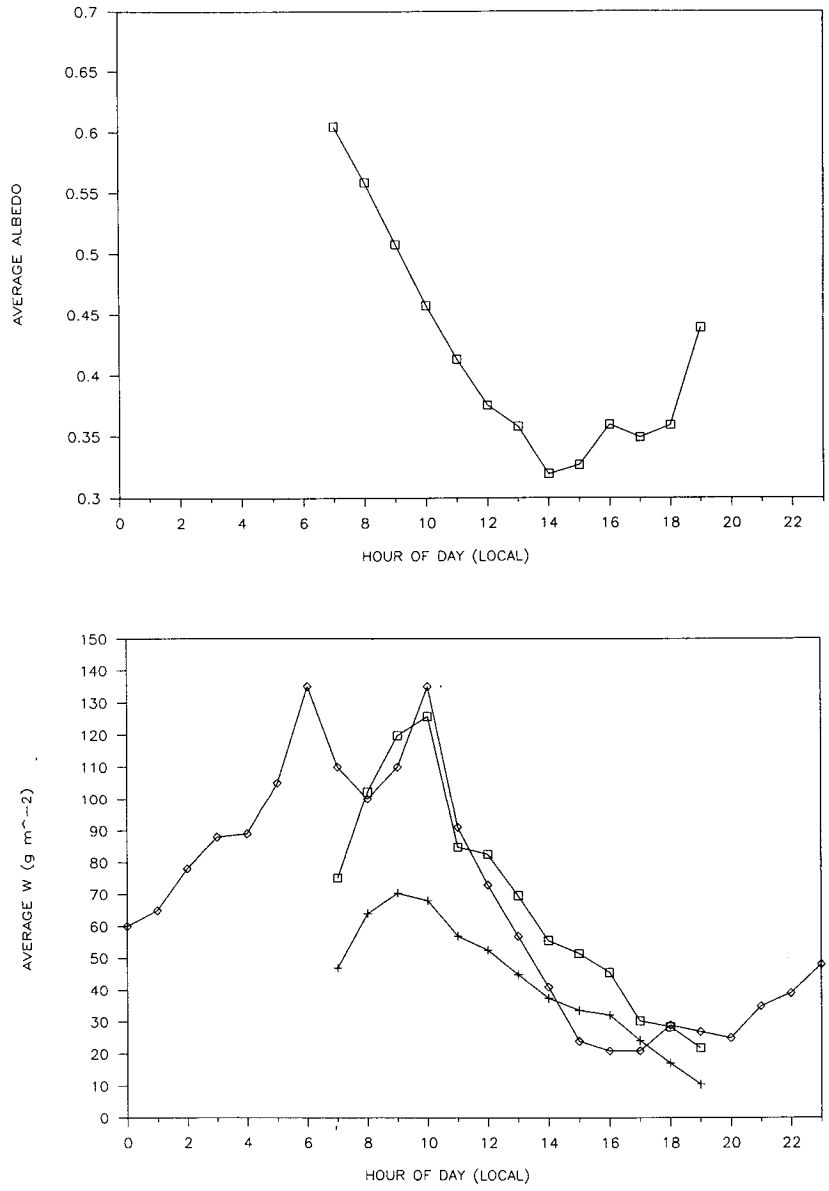

FIG. 16. As in Fig. 15 but using shortwave irradiance derived values of (a) cloud albedo, and (b) integrated cloud liquid water. In Fig. 16b the diamond symbols denote microwave radiometer measurements of W.

the day. The microwave radiometer provides far superior performance for measuring W, but at a somewhat greater cost than a pyranometer.

The SNI data have revealed some interesting information on the stratocumulus regime during the eight-month period studied. Frequency distributions indicate the stratocumulus at SNI had a cloud base on the order of 400 m, an integrated liquid water content of 75 g m^{-2}, and an albedo of 0.55. As expected, substantial diurnal variations were found. The mean cloud cover for the three summer months peaked at 0.74 at sunrise and was a minimum of 0.41 at sunset. The integrated cloud liquid water content declined nearly a factor of 2 during the seven hours of primary solar heating. This is actually a weaker diurnal variation than that observed with the microwave radiometer during the FIRE IFO. This suggests that the IFO period is not completely representative of the entire summer.

The applicability of these results to the entire stratocumulus regime of the eastern Pacific has not been established yet. The island itself is known to influence the local cloud structure, even causing local clearing at times. The position of the sensors on a low point on the upwind extreme of the island greatly reduces these

effects. Visual observations during the FIRE IFO indicate that the clouds at the northwest tip of the island were quite representative of those farther upwind of this island, even when the bulk of the island had cleared a hole in the clouds. However, it is unrealistic to assume that island influence is totally absent from this dataset. Also, SNI is more representative of the California coastal regime than the open ocean. Satellite observations (Young et al. 1989) have indicated higher cloud albedo near the coast, possibly due to the greater concentrations of cloud condensation nuclei associated with the continent and the pollution plume from the Los Angeles basin. This could explain the 30% higher cloud optical thicknesses discussed above. Analysis of satellite data and FIRE IFO aircraft data should shed some light on this issue. Direct comparisons of satellite and SNI in situ observations are also being evaluated.

Acknowledgments. This work is supported by the NASA Grant NAG 1-652. Part of this work was performed while CWF was a visiting scientists at the Naval Environmental Prediction and Research Facility. The authors wish to express special thanks to Richard Dixon and Carl Otten of PMTC for aiding in the installation and maintainence of the ETO system at SNI; to Dick Thompson of the Department of Meteorology, PSU, who put the system together and kept the data flowing; and to Bruce Albrecht, Craig Bohren, and Tom Ackerman for comments on the manuscript.

REFERENCES

Albrecht, B. A., D. A. Randall and S. Nicholls, 1988: Observations of marine stratocumulus clouds during FIRE. *Bull. Amer. Meteor. Soc.*, **69,** 618–626.

——, C. W. Fairall, D. W. Thomson, A. B. White, J. B. Snider and W. H. Schubert, 1990: Surface based remote sensing of the observed and the adiabatic liquid water content of stratocumulus clouds. *Geophys. Res. Lett.*, **17,** 89–92.

Blanc, T. V., 1981: Report and analysis of the May 1979 Marine Surface Layer Micrometeorological Experiment at San Nicolas Island, California. NRL Rep. 8363, Naval Research Laboratory, Washington, DC, 149 pp. [NTIS ADA 110488.]

Brunt, D., 1932: Notes on radiation in the atmosphere. *Quart. J. Roy. Meteor. Soc.*, **58,** 389–420.

Charlson, R. J., J. E. Lovelock, M. O. Andreae and S. G. Warren, 1987: Oceanic phytoplankton atmospheric sulphur, cloud albedo and climate. *Nature,* **326,** 655–661.

Coakley, J. A., and P. Chylek, 1975: The two stream approximation in radiative transfer: Including the angle of the incident radiation. *J. Atmos. Sci.*, **32,** 409–418.

Coakley, J. A., Jr., and F. P. Bretherton, 1982: Cloud cover from high resolution scanner data: Detecting and allowing for partially filled fields of view. *J. Geophys. Res.*, **87,** 4917–4932.

——, and D. G. Baldwin, 1984: Towards the objective analysis of clouds from satellite imagery data. *J. Climate Appl. Meteor.*, **23,** 1065–1099.

Cox, S. K., D. McDougal, D. Randall and R. Shiffer, 1987: FIRE—the First ISCCP Regional Experiment. *Bull. Amer. Meteor. Soc.*, **67,** 114–118.

Davidson, K. L., C. W. Fairall, P. Jones Boyle and G. E. Schacher, 1984: Verification of an atmospheric mixed-layer model for a coastal region. *J. Climate Appl. Meteor.*, **23,** 617–636.

Fravalo, C., Y. Fouquart and R. Rosset, 1981: The sensitivity of a model of low stratiform clouds to radiation. *J. Atmos. Sci.*, **38,** 1049–1062.

Frouin, R., C. Gautier and J. Morcrette, 1988: Downward longwave irradiance at the ocean surface from satellite data: Methodology and in situ validation. *J. Geophys. Res.*, **93,** 597–619.

Gautier, C., G. Diak and S. Masse, 1980: A simple physical model to estimate incident solar radiation at the surface from GOES satellite data. *J. Appl. Meteor.*, **19,** 1005–1012.

Hogg, D. C., F. O. Guiraud, J. B. Snider, M. T. Decker and E. R. Westwater, 1983: A steerable dual-channel microwave radiometer for measurement of water vapor and liquid in the atmosphere. *J. Appl. Meteor.*, **22,** 789–806.

Lilly, D. K., 1968: Models of cloud-toppped mixed layers under a strong inversion. *Quart. J. Roy. Meteor. Soc.*, **94,** 292–309.

Minnis, P., and E. F. Harrison, 1984: Diurnal variability of regional cloud and clear-sky radiative parameters derived from GOES data, II, November 1978 cloud distributions. *J. Climate Appl. Meteor.*, **23,** 1012–1031.

——, and B. A. Wielicki, 1988: Comparison of cloud amounts derived using GOES and Landsat data. *J. Geophys. Res.*, **93,** 9385–9403.

——, —— and G. G. Gibson, 1987: Cloud cover over the equatorial eastern Pacific derived from July 1983 International Satellite Cloud Climatology Project data using a hybrid bispectral threshold method. *J. Geophys. Res.*, **92,** 4051–4073.

Payne, R. E., 1972: Albedo of the sea surface. *J. Atmos. Sci.*, **29,** 959–970.

Randall, D. A., J. A. Abeles and T. G. Corsetti, 1985: Seasonal simulations of the planetary boundary layer and boundary-layer stratocumulus clouds with a general circulation model. *J. Atmos. Sci.*, **42,** 641–676.

——, J. A. Coakley, Jr., C. W. Fairall, R. A. Kropfli and D. H. Lenschow, 1984: Outlook for research on subtropical marine stratiform clouds. *Bull. Amer. Meteor. Soc.*, **65,** 1290–1301.

Schubert, W. H., S. K. Cox, P. E. Ciesielski and C. M. Johnson-Pasqua, 1987: Operation of a ceilometer during the FIRE marine stratocumulus experiment. Colorado State University Atmospheric Science Pap. No. 420, 101 pp.

Siegel, D. A., and T. D. Dickey, 1986: Variability of net longwave radiation over the eastern north Pacific Ocean. *J. Geophys. Res.*, **91,** 7657–7666.

Simpson, J. J., and C. A. Paulson, 1979: Mid-ocean observations of atmospheric radiation. *Quart. J. Roy. Meteor. Soc.*, **105,** 487–502.

Snider, J. B., 1988: Verification of the accuracy of a network of water vapor radiometers. *Proc. of IGARSS 88 Symp.*, Edinburgh, Scotland, 19–20. [Available from IEEE, pub. #88CH2497-6, PO Box 1331, Piscataway, NJ, 08855-1331.]

Stephens, G. L., 1978: Radiation profiles in extended water clouds. II: Parameterization schemes. *J. Atmos. Sci.*, **35,** 2123–2132.

——, S. Ackerman and E. A. Smith, 1984: A shortwave parameterization revised to improve cloud absorption. *J. Atmos. Sci.*, **41,** 687–690.

Young, D. F., P. Minnis and E. F. Harrison, 1989: Satellite-derived cloud and radiation fields over the marine stratocumulus IFO. *Proc. FIRE Science Meeting,* Monterey, 83–87. [Available from the FIRE Project Office, NASA Langley Research Center, Hampton, VA 23665-5225.]